Sub-Nyquist underwater denoising ghost imaging with a Coiflet-wavelet-order-based Hadamard matrix

Heng Wu,[1,2,*] Genping Zhao,[1,2,*] Chunhua He,[1,2,†] Lianglun Cheng,[1,2] and Shaojuan Luo[3,‡]
[1]*Guangdong Provincial Key Laboratory of Cyber-Physical System, School of Automation, Guangdong University of Technology, Guangzhou, 510006, China*
[2]*School of Computer, Guangdong University of Technology, Guangzhou, 510006, China*
[3]*School of Chemical Engineering and Light Industry, Guangdong University of Technology, Guangzhou 510006, China*

(Received 25 July 2022; accepted 15 November 2022; published 28 November 2022)

Underwater ghost imaging (GI) plays an important role in the marine research, marine environment protection, and engineering applications. However, underwater GI encounters the challenges of numerous measurements and noise interference caused by the scattering lights. To solve these problems, we propose a sub-Nyquist denoising GI method to acquire high-quality images of the underwater objects. The proposed method first uses a Coiflet-wavelet decomposition method to create an index order and then utilizes the order to reorder the Hadamard pattern sequence. Then, a total variation regularization algorithm is designed to restore the object images, and a nuclear-norm-minimization algorithm is developed to remove the noises from the restored images. Finally, an experimental setup is built to simulate the complicated underwater environment that includes the turbulence and bubbles. The numerical and experimental results show that the denoising capability of the proposed method is strong, and the imaging performance of the proposed method is similar (slightly better in some cases) to the recently reported state-of-the-art GI methods in the complicated underwater environment and sub-Nyquist sampling ratio condition (e.g., 0.03). The proposed method may find applications in marine underwater imaging areas.

DOI: 10.1103/PhysRevA.106.053522

I. INTRODUCTION

Underwater imaging (UI) technology is essential for the underwater research and engineering applications [1–4]. Due to the water absorption and scattering of lights, UI techniques [5–7] face the problems of noise interference, low contrast, limited imaging distance, etc. Underwater ghost-imaging (GI) technique is an alternative for the traditional UI and has been utilized in UI over the past few years [8–10]. Unlike the conventional UI methods, e.g., the deep-learning UI [11,12], cross-talk compensation UI [13], metalens-based UI [14], etc., GI is a nonlocal indirect imaging technique [15–20] and can be used to reconstruct the images of objects in scattering medium [21–23], low-light environment [24], turbid media [25–27], and so on. Moreover, GI can also recover an object image with multiple spectra [28]. Owing to the above advantages, GI has great application prospect in the UI area.

Recently, many works on the underwater GI (UGI) have been presented. Gao *et al.* reported that the image resolution of UGI could be improved by increasing the liquid refractive index of the transparent liquid [29]. Zhang *et al.* found [30] that GI could produce better image quality than the traditional imaging technique in the seawater environment. Zhao *et al.* proposed a push-broom UGI method [31], where the GI images are recovered by an iterative shrinkage thresholding algorithm. This method could effectively reduce the backscattering. Luo *et al.* used a shaped Lorentz source for the underwater illumination, and high-quality GI images could be obtained even if the imaging distance is quite long [32]. Wang *et al.* introduced a compressive sensing (CS) UGI method, where a wavelet enhancement algorithm is used to further enhance the quality of the restored images [33]. This method can acquire clear images for underwater objects with a sub-Nyquist sampling ratio. Yang *et al.* demonstrated a UGI scheme based on the generative adversarial networks [34]. The experimental and simulation results indicate that this scheme effectively improves the image quality of UGI. Moreover, the impacts of the water turbidity on the imaging performance of UGI have aroused wide concerns. Bina *et al.* demonstrated that the backscattering differential GI method could achieve better contrast than the direct imaging scheme in turbid media [27]. Le *et al.* studied the image quality of UGI in different turbidities and angles [35]. The results show that GI is not sensitive to the water turbidity changes. Yuan *et al.* developed a GI method to imaging objects hidden in the turbid media [25]. This method is not limited by the object size. Besides, the influence of the water turbulence to the UGI are also studied. For instance, Yin *et al.* showed that GI had the turbulence-free ability in the conditions of the low temperature, vibration, and turbidity of water [36]. Zhang *et al.* investigated the imaging performance of GI in the oceanic turbulence condition [37]. They found that the turbulence intensity and imaging distance have significant

*These authors contributed equally to this work.
†hechunhua@pku.edu.cn
‡kesjluo@gdut.edu.cn

 ©2022 American Physical Society

impacts on the image quality of UGI. Wu *et al.* reported the antidisturbance ability of UGI, and the results showed that UGI is superior to the conventional imaging method in the underwater disturbance condition [38]. Additionally, Liu *et al.* presented a UGI method in the oceanic turbulence by using a partially coherent beam [39]. They found that the quality and visibility of the GI image are less affected by their method.

In Hadamard ghost imaging, the selection of patterns has great influence on the quality of the recovered images in sub-Nyquist sampling conditions [40–44]. Over the past few years, many methods have been proposed to choose the patterns from the Hadamard matrix by using the specially designed orders, such the total gradient ascending order (TG) [42], "cake cutting" (CC) [43], ascending scale (AS) [44], and so on. The Coiflet wavelet (CW) has the properties of the near-symmetric, orthogonal, and biorthogonal, which is widely used in the digital signal processing. In the image-processing area, the CW coefficients of an image can be obtained by the wavelet decomposition method. From numerous numerical and actual experiments, we find that the CW coefficients can be used to reorder the Hadamard pattern sequence, and high-quality ghost images can be produced with a usb-Nyquist sampling ratio (e.g., 0.05 and 0.07) by using the reordered patterns. Consequently, the CW coefficients can help to decrease the measurements in GI.

To reduce measurement numbers and enhance the image quality of UGI, we present a sub-Nyquist underwater Hadamard GI method by using a CW decomposition method and a CS-nuclear-norm-minimization algorithm. We propose a CW order that is used to reorder the Hadamard pattern sequence by a wavelet decomposition method. The CS combining with the nuclear-norm-minimization (NNM) algorithm is utilized for the object image reconstruction. The effectiveness of the proposed CW order is verified by comparing with six previous reported Hadamard orders. Moreover, seven GI methods are used to compare the imaging performance of the proposed method. Numerical and actual experiments are implemented to show the effectiveness and advantages of the proposed method.

II. METHOD

A. Imaging system

The configuration of the imaging system is shown in Fig. 1. The imaging system is controlled by a personal computer (PC). The PC sends a Hadamard pattern sequence (HPS) R to a light-modulation device (LMD) which is used to modulate the light beam, and then records the corresponding light-intensity sequence (LIS)D collected by a bucket detector (BD). Three lenses are installed in the system, where the PL (projective lens) is utilized to project the modulated light to the target; L1 and L2 are used to converge the light beam. Here, the HPS and LIS are, respectively, defined as

$$R = [R_1(x, y), R_2(x, y), \cdots, R_K(x, y)], \tag{1}$$

$$D = [D_1, D_2, \cdots, D_K], \tag{2}$$

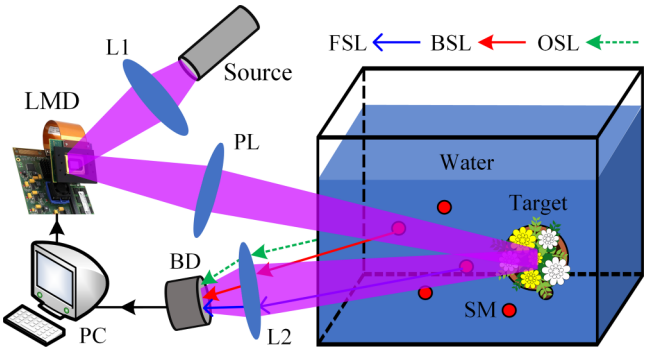

FIG. 1. Schematic plot of the imaging system. L1, lens 1; L2, lens 2; LMD, light modulation device; PL, projective lens; BD, bucket detector; PC, personal computer; SM, suspended microparticles; BSL, backscattering light; FSL, forward-scattering light; OSL, other stray light.

where the light intensity D_k in the LIS is obtained by [15,18,45]

$$I_k = \iint R_k(x, y)O(x, y)dxdy + \Psi, \tag{3}$$

where $R_k(x, y)$, $O(x, y)$, K, Ψ, and (x, y) are the Hadamard pattern, object function, total Hadamard pattern number, noise interference, and pixel coordinate, respectively, $k = 1, 2, \cdots, K$. Here, the target $O(x, y)$ is placed in the water that contains many suspended microparticles (SMs). Thus, the noise interference Ψ mainly includes three parts, the backscattering light (BSL), other stray light (OSL), and forward-scattering light (FSL).

In Eq. (1), the Hadamard pattern $R_k(x, y)$ is produced by

$$R_k(x, y) = reshape(G_k, [Q, Q]), \tag{4}$$

where G_k is the kth row of the Hadamard matrix (HM) G, and Q is the size of the Hadamard pattern. Note that the HM is created by $G = \text{hadamard}(V)$, where G is a $V \times V$ matrix. Here, hadamard() and *reshape*() are MATLAB functions, $V = Q \times Q$. The *reshape*() function is used to turn G_k into a $Q \times Q$ matrix.

As the $R_k(x, y)$ consists of $+1$ and -1, a differential method is used to change the -1 into $+1$, $R_k(x, y) = R_k{}^+(x, y) - R_k{}^-(x, y)$, where $R_k{}^+(x, y) = [R_k(x, y) + 1]/2$ and $R_k{}^-(x, y) = 1 - R_k{}^+(x, y)$ are composed of 0 and $+1$. Consequently, each Hadamard pattern $R_k(x, y)$ is divided into two patterns that can be shown in the LMD.

B. Generation of the Coiflet-wavelet order

With Sec. II A, a HPS that is composed of the patterns $R_k^+(x, y)$ and $R_k^-(x, y)$ is generated. As illustrated in the third paragraph of the Introduction, the CW coefficients can be applied to reorder HPS and reduce the measurements in GI. Thus, a CW decomposition-based method is proposed to rearrange the HPS. The proposed method first uses a CW decomposition method to calculate the CW coefficients of each pattern in the HPS and obtains a final CW coefficient value corresponding to each pattern by summing the relative CW coefficients. Therefore, a CW coefficient value sequence corresponding to the HPS is produced. Then, the CW

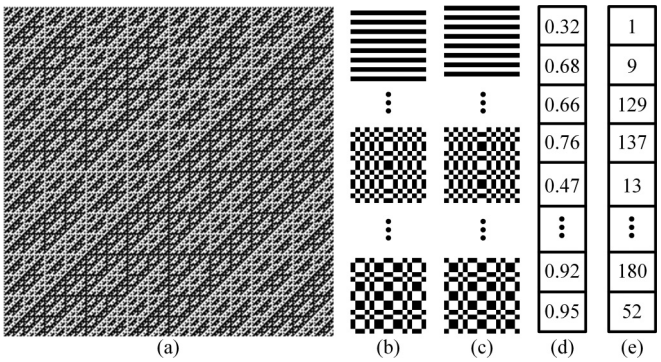

FIG. 2. Example of the CW order generation. (a) Original Hadamard matrix; (b), (c) Hadamard patterns, respectively, produced by reshaping the rows of (a) and differential method (d) total coefficients, and (e) index array.

coefficient value sequence is sorted in an ascending order and a sorted index is acquired. Finally, the HPS is rearranged with the sorted index. The implementation process of the proposed method is detailed as follows.

Firstly, all the positive ones (+1) in the $R_k^+(x,y)$ and $R_k^-(x,y)$ are set as 255, which turns the pattern matrix into images. This step is the data preprocessing which is used to prepare images for computing the wavelet coefficients with program languages. Secondly, the wavelet coefficients C_k^+ and C_k^- corresponding to the $R_k^+(x,y)$ and $R_k^-(x,y)$ are, respectively, calculated by a decomposition method:

$$C_k^{\pm}(\alpha,\beta) = \iint R_k^{\pm}(u,v)\varphi(\alpha-u,\beta-v)dudv, \qquad (5)$$

where $\varphi(\cdot)$ denotes the Coiflet-wavelet basis function; α and β are the shift factors. Here, Eq. (5) is solved by $C_k^{\pm} =$ wavedec2($R_k^{\pm}(x,y)$,H, $'$coif1$'$), where wavedec2() is a MATLAB function, H and $'$coif1$'$ are the wavelet decomposition level and wavelet type, respectively. This step is utilized to generate the CW coefficients of each pattern in the HPS. Thirdly, the total coefficients are computed by $C_k = |C_k^+| + |C_k^-|$, where $|\cdot|$ is the absolute value function. By this way, each pattern is corresponding to a final CW coefficient value C_k. Finally, when all the coefficients of the HPS are acquired, the coefficient sequence is ranged in an ascending order, and the corresponding index array S_{index} of the sorted coefficient sequence is obtained. With S_{index}, the HPS R is rearranged. Note that the HPS obtained by the sorted CW coefficient sequence is named the CW order HPS. By using the CW order HPS, high-quality ghost images can be restored. These will be verified by experiments in Sec. III A.

Figure 2 shows an example of the proposed CW order, where $Q = 16$ and $V = 256$. Figure 2(a) exhibits the original HM (256 × 256 pixels), where the −1 and +1 in the matrix are set as 0 and 255, respectively. Figures 2(b) and 2(c) present the images $R_k^+(x,y)$ and $R_k^-(x,y)$, respectively. The sizes of images in Figs. 2(b) and 2(c) are 16 × 16 pixels. Figure 2(d) is the total coefficients calculated from Figs. 2(b) and 2(c). Figure 2(e) is the final CW order corresponding to the sorted coefficients in Fig. 2 (d).

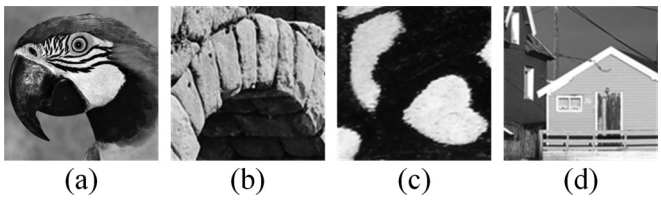

FIG. 3. Objects for simulations.

C. Compressive image reconstruction

A total variation (TV) regularization-based CS algorithm is designed for the image reconstruction [46]. Although the running speed of this algorithm is slower than the widely used TVAL3 algorithm [47], the parameter setting of this algorithm is fewer and the quality of the reconstructed image is better. The image reconstruction of this algorithm is achieved by solving the following optimization model:

$$\min \|Y\|_1, \ \textit{subject to}\ \Phi X = Y \ \textit{and}\ \Theta X = D, \qquad (6)$$

Where Y, D, and Φ are the gradient of the object image, LIS, and gradient calculation matrix, respectively. X, Θ, and $\|\cdot\|_1$ are the restored object image, measurement matrix, and l_1 norm, respectively.

D. Image denoising with nuclear-norm minimization

The NNM is developed to reduce the noises in the image X restored by the CS method in Sec. II C. The mathematical model of the NNM denoising method is expressed as

$$\arg\min_U \|Z-U\|_F^2 + \lambda\|U\|_{w,*}, \qquad (7)$$

where $\|\cdot\|_F$ is the F norm; $\|\cdot\|_{w,*}$ is the nuclear norm with weight vector w; Z, U,and λ are the observed data matrix, latent data matrix, and positive constant, respectively. Here, the observed data matrix Z is set as the restored image X. The weighted NNM denoising algorithm in Ref. [48] is set as the solver for Eq. (7).

After denoising by Eq. (7), the final image is output.

III. SIMULATIONS

A. Performance comparison of different orders

This simulation is designed to compare the imaging performance of the proposed CW order with that of the six state-of-the-art Hadamard orders. The "bird" and "bridge arch" (128 × 128 pixels) are used as the object, as shown in Figs. 3(a) and 3(b). The image reconstruction algorithm is the correlation calculation [15,18,20], expressed as $O(x,y) = \langle RD\rangle - \langle R\rangle\langle D\rangle$, where $\langle\cdot\rangle = \frac{1}{K}\sum_{k=1}^{K}\cdot$ denotes the assemble average. Note that the correlation calculation algorithm can objectively reflect the performance of each Hadamard order because no special parameters are needed to set in this algorithm. The images restored with different sampling ratios (0.03, 0.05, 0.07, and 0.09) are shown in Fig. 4. Here, the sampling ratio (SR) is defined as SR $= A/(Q\times Q)$, where A is the actual measurement number. The seven comparison Hadamard orders are the TG [42], CC [43], AS [44], sequency ordering combining with the zigzag traversal (GCSS) [49], total variation (TV) [42,50], ascending inertia (AI) [44], and proposed CW (Pro) order.

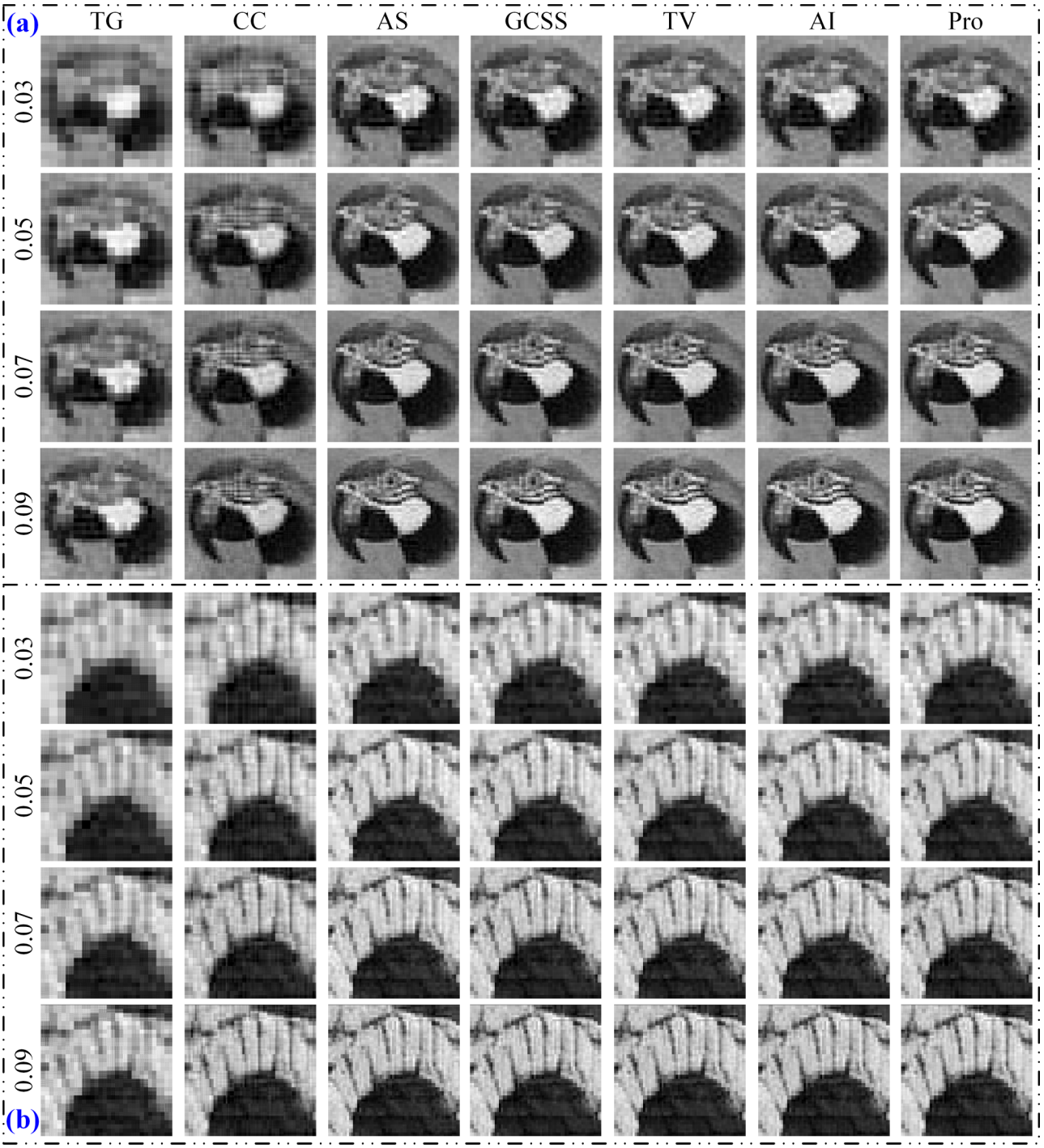

FIG. 4. Simulation results of targets (a) bird and (b) bridge arch under different sampling ratios.

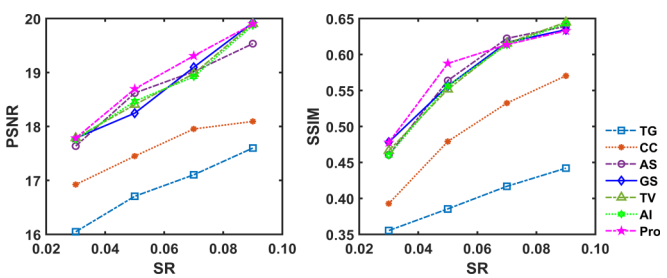

FIG. 5. PSNR and SSIM of images in Fig. 4(a).

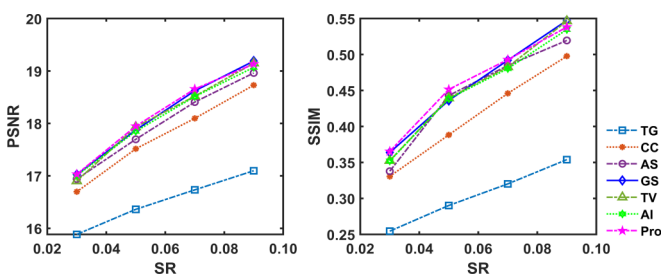

FIG. 6. PSNR and SSIM of images in Fig. 4(b).

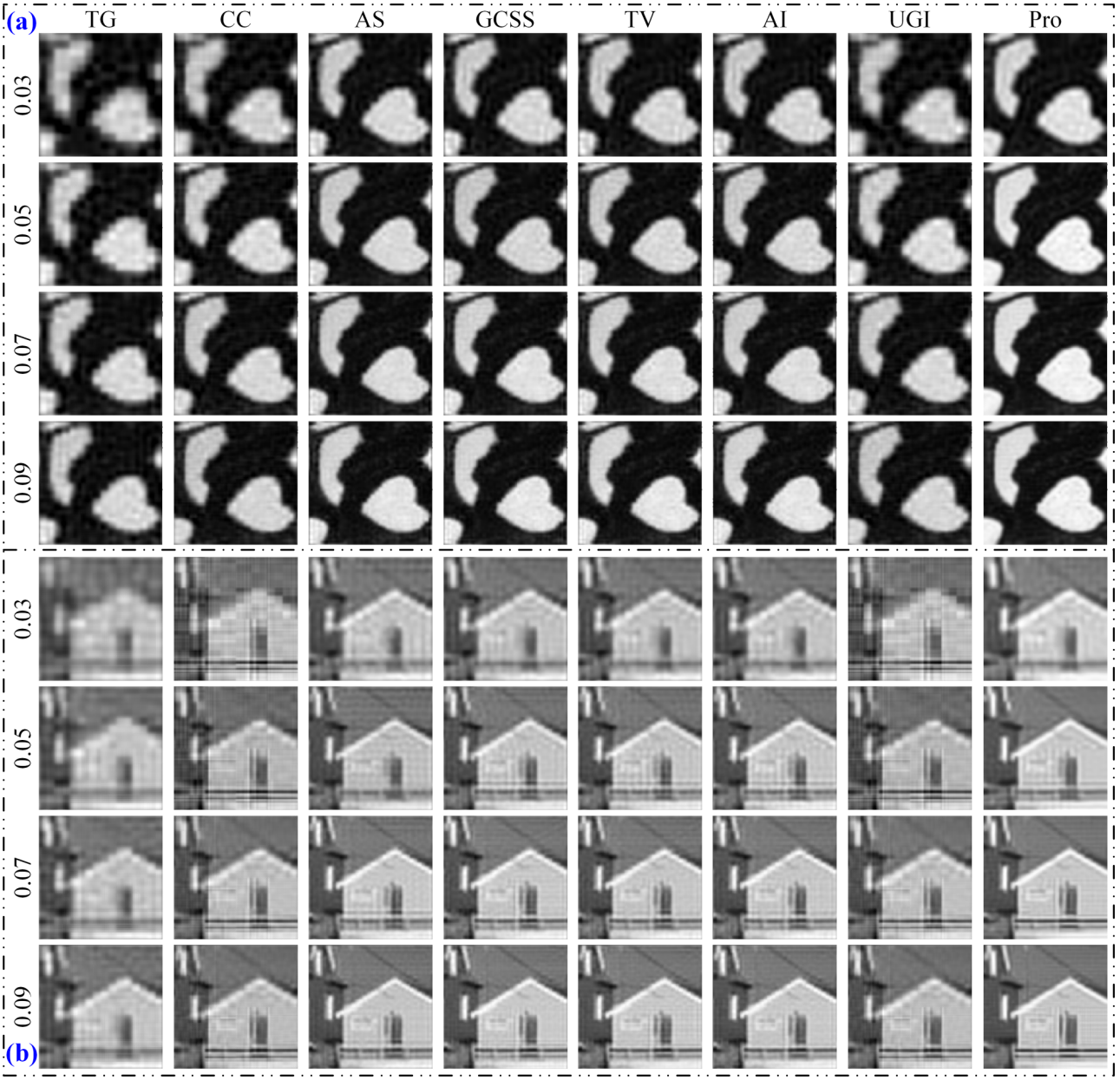

FIG. 7. Simulation results of targets (a) white block and (b) house with different sampling ratios.

As displayed in Fig. 4, from the perspective of the direct vison, the image quality of AS, GCSS, TV, AI, and Pro is close to each other and better than that of the TG and CC when the SR increases from 0.03 to 0.09. The details of the recovered images (from AS to Pro) become clearer with the increasing of SR. For instance, the eyes of the birds are quite clear and textures of bridge arch are quite distinct when the SR is 0.07. The peak signal-to-noise ratio (PSNR) [51] and Structural SIMilarity (SSIM) index [52] are used to quantitatively compare the quality of the restored images. Figures 5 and 6 display the comparison results of PSNR and SSIM, where Figs. 5(a) and 5(b) are corresponding to the images in Fig. 4(a); Figs. 6(a) and 6(b) are corresponding to the images in Fig. 4(b). As shown in Figs. 5(a) and 5(b), TG gains the worst PSNR and SSIM. The PSNR and SSIM of CC are better than TG, but worse than those of the other five methods (from AS to Pro). The PSNR and SSIM of the mentioned five methods are quite close. However, the PSNR and SSIM of Pro are superior to the others when the SR is equal to 0.03 and 0.05. When the SR is equal to 0.07 and 0.09, the SSIM of Pro is a little worse than the others. Nonetheless, from the point of view of the comprehensive performance in Figs. 4, 5, and 6, the proposed CW order is slightly better than the other six orders in the sub-Nyquist SR conditions (e.g., SR = 0.03 and 0.05).

B. Performance comparison of different methods

1. Simulation 1

In this simulation, the imaging performance of the proposed method (Pro) is compared with the other seven

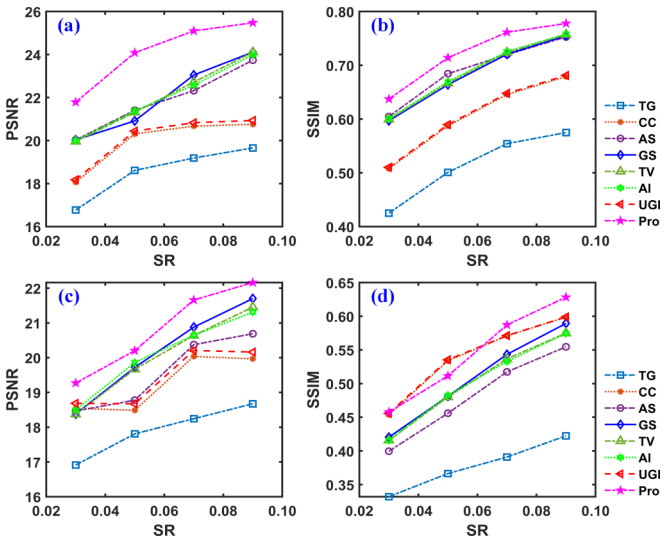

FIG. 8. (a) PSNR and (b) SSIM of images in Fig. 7(a). (c) PSNR and (d) SSIM of images in Fig. 7(b).

methods. Here, the methods include the six methods in Sec. III A. Note that the image reconstruction algorithms of the six methods are reproduced according to the original paper [42–44,49,50]. Besides, the wavelet enhancement-based underwater GI is also used for comparison [33], simplified as UGI. The targets "white block" and "house" (128 × 128 pixels) are utilized for simulations, as shown in Figs. 3(c) and 3(d). The results of the eight methods are exhibited in Fig. 7. When the SR goes from 0.03 to 0.09, the image quality of Pro is better than that of TG and CC, and close to the other five methods. As shown in Figs. 7(a) and 7(b), when the SR is equal to 0.05, AS, GCSS, TV, AI, and Pro can output high-quality images. But, as for the CC and UGI, two unexpected slits are produced at the bottom of the restored images in Fig. 7(b) when the SR is 0.03 and 0.05. The two slits disappear as the SR increases to 0.07 and 0.09.

The PSNR and SSIM of images in Fig. 7 are plotted in Fig. 8, where Figs. 8(a) and 8(b) are the results of Fig. 7(a); Figs. 8(c) and 8(d) are the results of Fig. 7(b). As shown in Fig. 8, apart from the SSIM of Pro in Fig. 8(d) when SR = 0.05, the PSNR and SSIM of Pro are superior to all the other methods, indicating that Pro gains the best image quality. In Fig. 8(d) when SR = 0.05, the SSIM of CC and UGI is better than that of Pro. This may be caused by the two unexpected slits. Comparing Pro with other methods in Fig. 7, the images of Pro look more smoothness and comfortable.

2. *Simulation 2*

In this simulation, Pro is compared with the other seven methods in the underwater environment. Here, the underwater noise is assumed to be the additive white Gaussian noise. The noises Ψ are generated by $\Psi = \text{awgn}(D, NL, '\text{measured}')$, where awgn(·) is a MATLAB function that is used to add the white Gaussian noise to signal, D and NL are the LIS and noise level, respectively. Note that the smaller the NL value, the heavier the noise. The simulation results are exhibited in Figs. 9 and 10, where the NL is set as 20. Compared with Fig. 7, the image sharpness decreases, and many noises appear in Figs. 9 and 10. Specifically, the image quality of TG is the worst among the eight methods. Except TG, the rest of the seven methods can obtain acceptable images. Nevertheless, from the perspective of the detail restoration, Pro is superior to all the other methods. For example, the northwest part of the white block (Fig. 9) and the door of the house (Fig. 10) are clearer than those of the other methods. The PSNR and SSIM of images in Figs. 9 and 10 are plotted

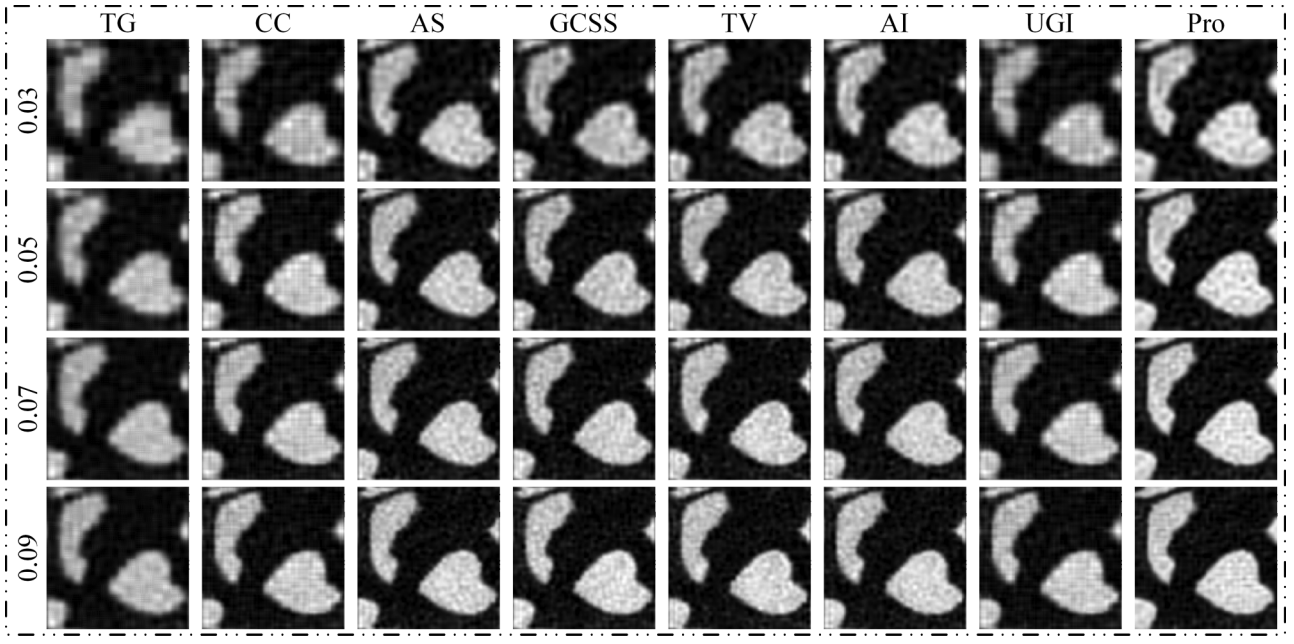

FIG. 9. Simulation results of the target white block under different sampling ratios with the noise level 20.

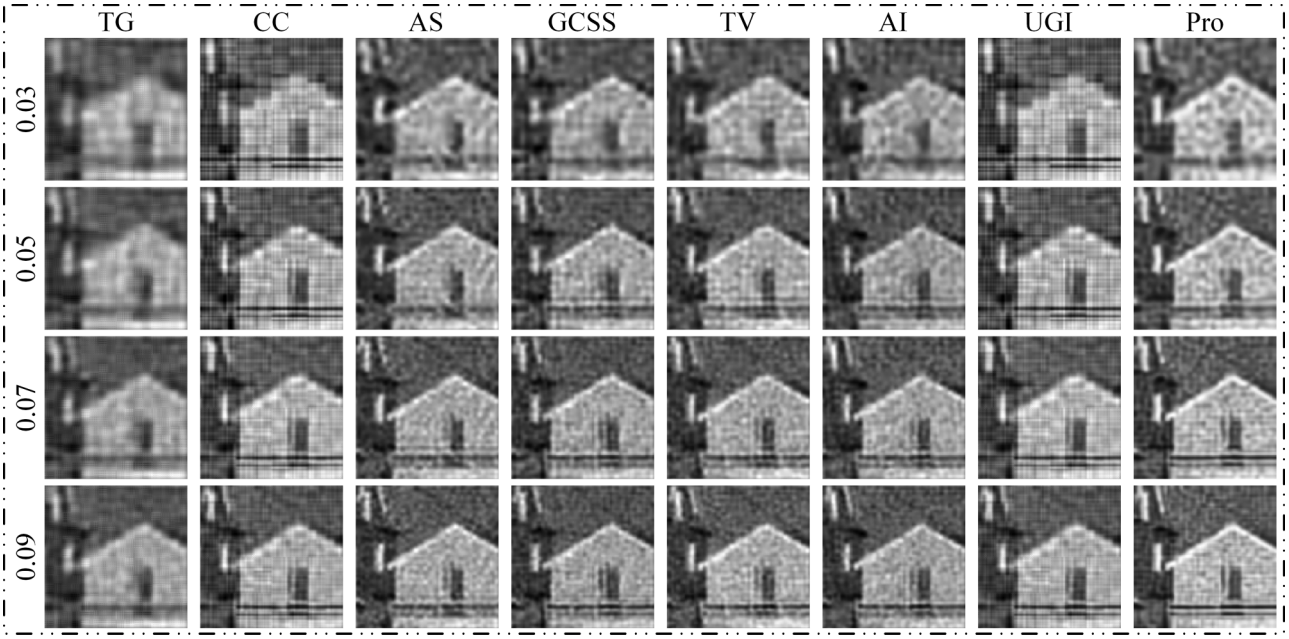

FIG. 10. Simulation results of the target house under different sampling ratios with the noise level 20.

in Fig. 11, where Figs. 11(a) and 11(b) are obtained from Fig. 9; Figs. 11(c) and 11(d) are calculated from Fig. 10. As shown in Figs. 11(a) and 11(b), the PSNR and SSIM of Pro are the best among the eight methods. However, Pro has the best PSNR in Fig. 11(c), but the SSIM of Pro is not the optimum in Fig. 11(d). This demonstrates that the noises break the structural similarity in the recovered images. Considering the details, sharpness, and evaluation index of the restored images, the imaging effect of Pro is the optimum among the eight methods.

As the simulation results shown in Figs. 4–11, the proposed CW order can help to reconstruct high-quality images with sub-Nyquist sampling ratios (e.g., 0.05 and 0.07), which is useful for reducing the measurement in Hadamard GI. Moreover, the image quality of Pro is superior to the mentioned seven GI methods. Besides, the simulation results indicate that Pro has strong denoising capability. The advantages of imaging with low SR and strong denoising capability are helpful for practical applications of Pro. The reasons are that many noises exist in actual environment, and a low SR can help to reduce the hardware requirement and improve the imaging efficiency.

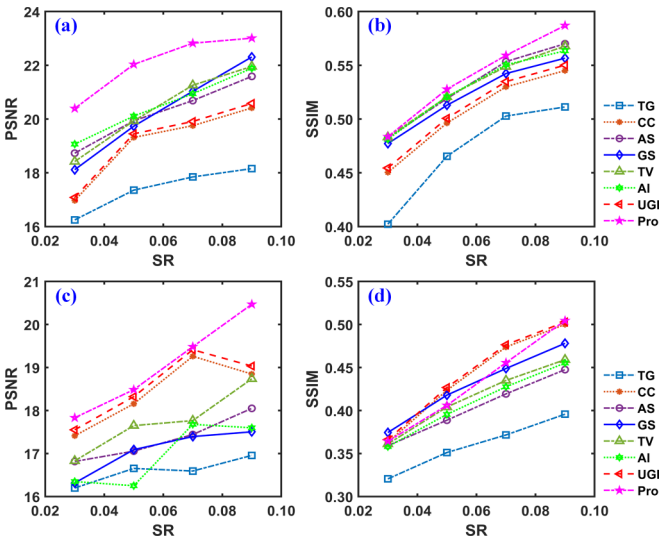

FIG. 11. (a) PSNR and (b) SSIM of images in Fig. 9. (c) PSNR and (d) SSIM of images in Fig. 10.

IV. EXPERIMENTS

An experimental system is built to verify the proposed method, as shown in Fig. 12. The LMD is a digital light projector (DLP, resolution 1920 × 1080 pixels, F4710 LC, Fldiscovery), which projects the illumination patterns to the

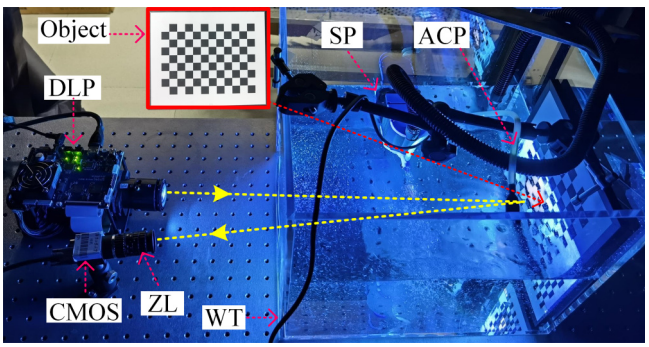

FIG. 12. Experimental system. ACP, air connection pipe; DLP, digital light projector; SP, submersible pump; WT, water tank; ZL, zoom lens; CMOS, complementary metal oxide semiconductor.

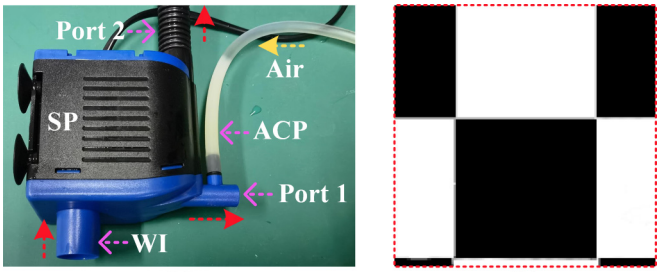

FIG. 13. (a) Structure of the submersible pump, (b) reference image. WI, water inlet.

object. The bucket detector is a complementary metal oxide semiconductor (CMOS) camera (Blackfly S BFS-U3-63S4C). The test object is a machine vision calibration board and is put into water. A zoom lens (focus length $f = 35$ cm) is mounted before the camera, which is used to gather the reflective light to the camera sensor.

A water tank (WT, refractive index1.49, size $45 \times 30 \times 30$ cm) is placed in front of the DLP and camera. Additionally, a submersible pump (SP) that is installed on the sidewall of WT is used to build the underwater turbulence and bubble environment. The SP has four ports: one water-inlet port, two water-outlet ports, and one air connection port, as shown in Fig. 13(a). The water from the two water outlets is circularly flowed around the WT, which produces a strong turbulence. A pipe is connected to the air-connection port. If the pipe is connected to the air, the SP can produce a great deal of bubbles. Otherwise, no bubble is generated. In the experiments, a PC is used to control the DLP and camera. Three groups of experiments are implemented. The configurations of each experiment are shown in Table I.

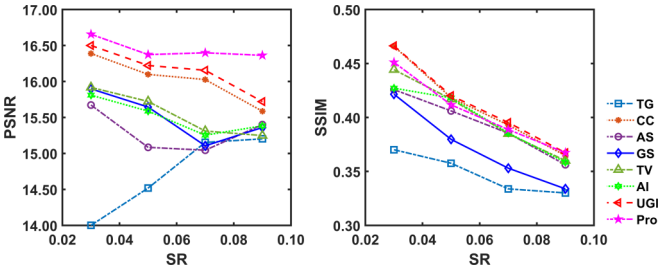

FIG. 15. PSNR and SSIM of images in Fig. 14.

A. Group 1: Without turbulence and bubbles

In this experiment, the SP is turned down, where no turbulence and bubbles are produced. Figure 14 shows the experimental results. Note that the resolution of the restored images in the three group experiments is all 128×128 pixels. As shown in Fig. 14, the recovered images of TG look a little blurred compared with the other seven methods. The image quality of the seven methods (from CC to Pro) looks nearly the same, which is hard to distinguish by the direct human vision. To quantitively evaluate the image quality of Pro, a refence image is created by ADOBE PHOTOSHOP. Figure 13(b) shows the created reference image, which is utilized for calculating the PSNR and SSIM. Figure 15 displays the PSNR and SSIM curves corresponding to images in Fig. 14. The PSNR of Pro is better than the other seven methods. Nevertheless, the SSIM curves of CC and UGI nearly overlap each other and are better than the rest of the methods. The SSIM curve of Pro is worse than that of CC and UGI when the SR is equal to 0.03, 0.05, and 0.07. When the SR is 0.09, the SSIM values of Pro, CC, and UGI perform almost the same. Additionally, as shown in Fig. 14, some noises appear in the restored images as the SR increases, resulting in a decreasing of the image quality.

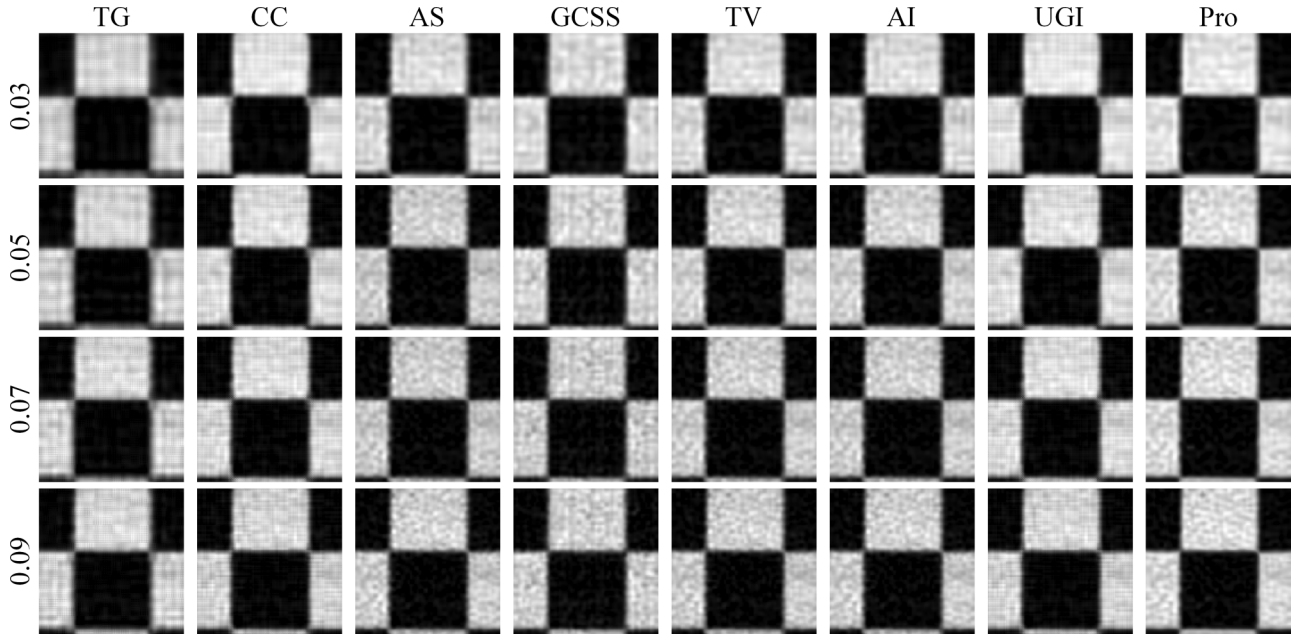

FIG. 14. Experimental results of the eight methods in the underwater environment, no turbulence and bubbles.

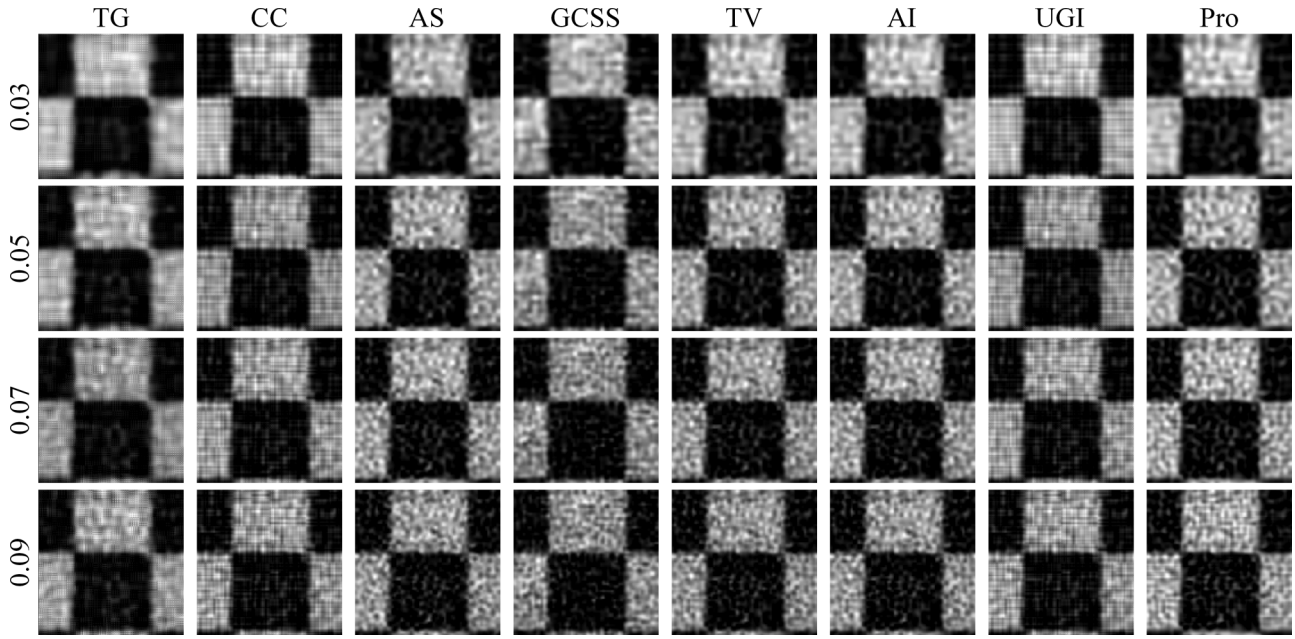

FIG. 16. Experimental results of the eight methods in the underwater environment, with turbulence and no bubbles.

These can also be seen from the PSNR and SSIM curves in Fig. 15. The reason may be that more measurements bring more underwater noises to the imaging data and degrade the image quality.

B. Group 2: With turbulence and no bubbles

In this experiment, the SP is turned on, and the air-connection pipe (ACP) is put into the water to stop the air coming in. Consequently, only the turbulence is created, and no bubbles are generated because of no air. Figure 16 exhibits the experiment results. The image-quality variation trend of each method in Fig. 16 is consistent with that of Fig. 14. Nonetheless, compared with Fig. 14, more noises appear in the recovered images of Fig. 16, indicating that the underwater turbulence reduces the quality of the image. The PSNR and SSIM curves of images in Fig. 16 are plotted in Fig. 17. The PSNR of Pro is still superior to the other seven methods, while the SSIM of Pro is quite bad. However, compared to the SSIM curves in Figs. 15 and 17, the SSIM curves of the eight methods in Fig. 17 get closer to each other, meaning that the structure difference of the restored images is small. When the SR is equal to 0.09, many noises are produced in the reconstructed images, the structures of the images look the same, and the images of Pro are a little lighter than those of the other methods. Considering the images in Fig. 16 and evaluation metrics in Fig. 17, the imaging performance of Pro is slightly better than the other methods.

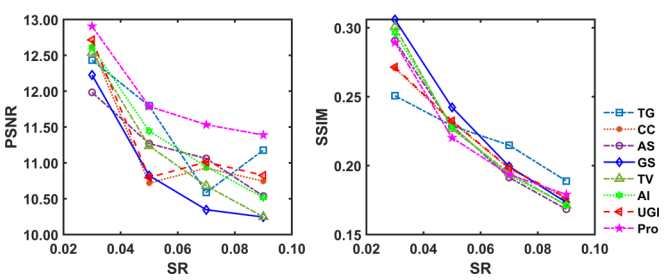

FIG. 17. PSNR and SSIM of images in Fig. 16.

C. Group 3: With turbulence and bubbles

In this experiment the SP is turned on, and the ACP is connected to the air. A strong turbulence and many bubbles are generated in the WT. The image reconstruction results of the eight methods are presented in Fig. 18. Comparing Fig. 18 with Figs. 14 and 16, the images of Fig. 18 contain more noises, and the image structures in Fig. 18 become worse than those in Figs. 14 and 16. Figure 19 shows the PSNR and SSIM curves of images in Fig. 18. When the SR is equal to 0.03, Pro gains the biggest PSNR values. However, when the SR is, respectively, equal to 0.05, 0.07, and 0.09, the PSNR of TG is the optimum. The SSIM values of all methods are lower than 0.3, meaning that the image structures are quite bad. As Figs. 18 and 19 show, the quality of the recovered images deteriorates seriously as the SR improves from 0.03 to 0.09. The main reasons lie in the following two aspects.

TABLE I. Experiment configurations.

Group	Adding turbulence?	Adding bubbles?
1	No	No
2	Yes	No
3	Yes	Yes

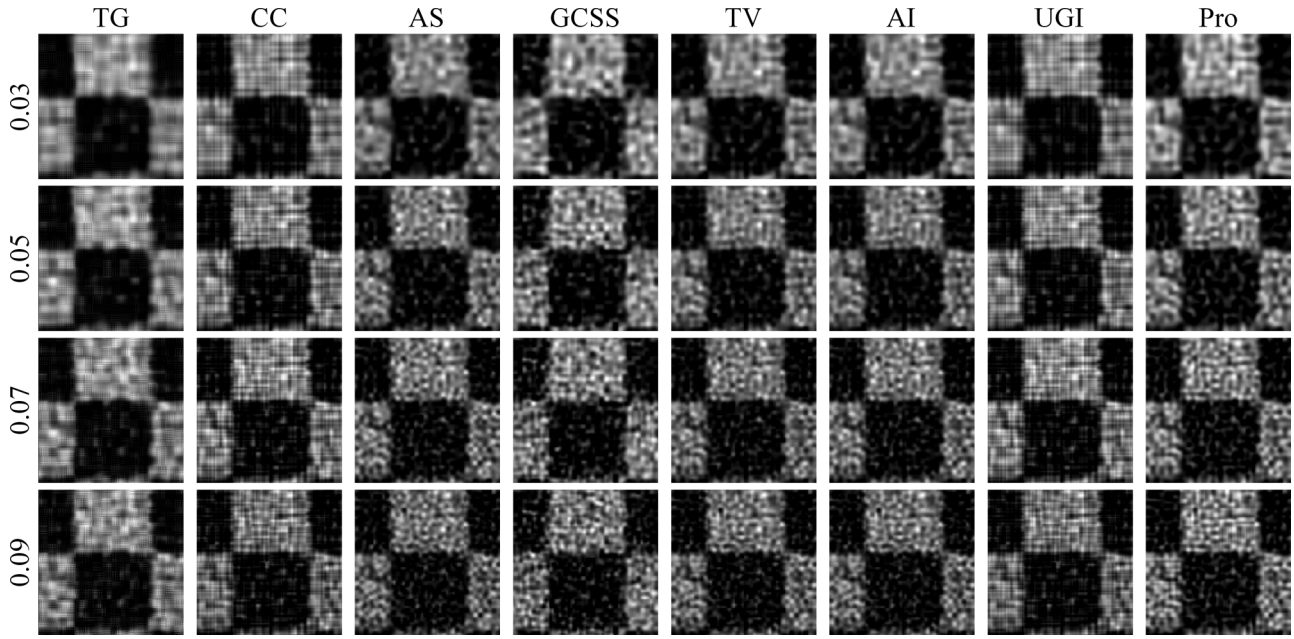

FIG. 18. Experimental results of the eight methods in the underwater environment, with turbulence and bubbles.

Firstly, the impurity tap water is used in the experiments. This kind of water contains many microparticles. The strong turbulence in the water can accelerate the random motion of microparticles. These generate many random scattered lights that reduce the image quality of GI methods. Secondly, the bubbles can also produce scattered lights. These scattered lights turn out to be noises during the GI image reconstruction and cause the degradation of the image quality for Pro and other GI methods.

As the results show in Figs. 14–19, Pro and other GI methods can obtain acceptable images in the underwater environment when the SR is equal to 0.03. With the increasing of SR, the image quality goes down. This means that a lower SR is helpful for underwater GI. Besides, the experiment results show that the turbulence and bubbles in the impurity water will lead to the degradation of GI images. From the numerical and experimental results in Secs. III and IV, Pro has a strong denoising capability and can restore high-quality images with a sub-Nyquist SR in the complicated underwater environment (e.g., turbulence and bubbles).

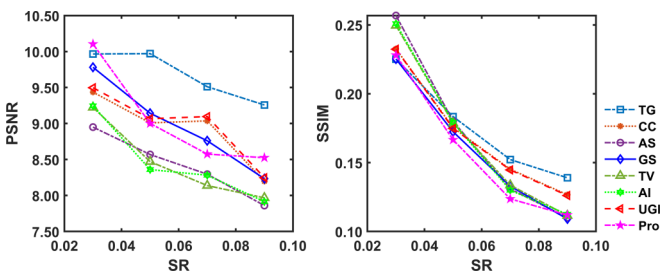

FIG. 19. PSNR and SSIM of images in Fig. 18.

V. CONCLUSION

We have proposed and presented a Hadamard GI method for imaging objects in the complicated underwater environment. A CW decomposition-based method (CW order) is proposed to create an optimized HPS. The CS and NNM algorithms are developed to restore high-quality images. The effectiveness and advantages of the proposed method are validated by three numerical simulations and three actual experiments. The numerical results show that the proposed CW order is superior to the previous Hadamard orders, e.g., TV, GCSS, AI, etc. The impact of underwater noises to the image quality of GI methods is also investigated. Both the numerical and experimental results demonstrate that the proposed method has strong denoising capability and performs similarly (slightly better in some cases) to existing best methods (e.g., CC, GCSS, AI, UGI, etc.) in sub-Nyquist SR conditions. As the underwater turbulence and bubbles degrade the image quality of GI methods, new methods will be designed to solve these problems in our future work. The proposed method offers an effective way to improve the image quality and imaging speed of underwater GI. In the future, we will develop deep learning-based methods to improve the image quality of UGI.

ACKNOWLEDGMENTS

The authors acknowledge the support of the National Natural Science Foundation of China (Grants No. 62173098, No. 62104047, No. U20A6003, No. U2001201, and No. 61805048), Key-Area Research and Development Program of Guangdong Province (Grant No. 2021B0101220001), and Guangdong Provincial Key Laboratory of Cyber-Physical System (Grant No. 2020B1212060069).

[1] M. K. Moghimi and F. Mohanna, Real-time underwater image enhancement: A systematic review, J. Real-Time Image Process. **18**, 1509 (2021).

[2] W. Gong, Performance comparison of computational ghost imaging versus single-pixel camera in light disturbance environment, Opt. Laser Technol. **152**, 108140 (2022).

[3] X. Ding, Y. Wang, and X. Fu, Multi-polarization fusion generative adversarial networks for clear underwater imaging, Opt. Laser Eng. **152**, 106971 (2022).

[4] J. Wang, M. Wan, G. Gu, W. Qian, K. Ren, Q. Huang, and Q. Chen, Periodic integration-based polarization differential imaging for underwater image restoration, Opt. Laser Eng. **149**, 106785 (2022).

[5] Z. Luo, Z. Tang, L. Jiang, and G. Ma, A referenceless image degradation perception method based on the underwater imaging model, Appl. Intell. **52**, 6522 (2022).

[6] P. Yang, H. Wu, S. Luo, and L. Cheng, Underwater image restoration using level adjustment and colour equalization, J. Mod. Opt. **69**, 817 (2022).

[7] Y. Shen, C. Zhao, Y. Liu, S. Wang, and F. Huang, Underwater optical imaging: Key technologies and applications review, IEEE Access **9**, 85500 (2021).

[8] H. Wu, M. Zhao, F. Li, Z. Tian, and M. Zhao, Underwater polarization-based single pixel imaging, J. Soc. Inf. Disp. **28**, 157 (2020).

[9] M. Wang, Y. Bai, X. Zou, M. Peng, L. Zhou, Q. Fu, T. Jiang, and X. Fu, Effect of uneven temperature distribution on underwater computational ghost imaging, Laser Phys. **32**, 65205 (2022).

[10] Q. Chen, A. Mathai, X. Xu, and X. Wang, A study into the effects of factors influencing an underwater, single-pixel imaging system's performance, Photonics **6**, 123 (2019).

[11] H. Hu, Y. Zhang, X. Li, Y. Lin, and T. Liu, Polarimetric underwater image recovery via deep learning, Opt. Laser Eng. **133**, 106152 (2020).

[12] Y. Zhu, T. Zeng, K. Liu, Z. Ren, and E. Y. Lam, Full scene underwater imaging with polarization and an untrained network, Opt. Express **29**, 41865 (2021).

[13] T. Liu, Z. Guan, X. Li, Z. Cheng, and H. Hu, Polarimetric underwater image recovery for color image with crosstalk compensation, Opt. Laser Eng. **124**, 105833 (2020).

[14] F. Zhao, R. Lu, X. Chen, C. Jin, S. Chen, Z. Shen, C. Zhang, and Y. Yang, Metalens-assisted system for underwater imaging, Laser Photonics Rev. **15**, 2100097 (2021).

[15] J. Cheng and S. Han, Incoherent Coincidence Imaging and Its Applicability in X-ray Diffraction, Phys. Rev. Lett. **92**, 093903 (2004).

[16] T. B. Pittman, Y. H. Shih, D. V. Strekalov, and A. V. Sergienko, Optical imaging by means of two-photon quantum entanglement, Phys. Rev. A **52**, R3429(R) (1995).

[17] H. Yu, R. Lu, S. Han, H. Xie, G. Du, T. Xiao, and D. Zhu, Fourier-transform Ghost Imaging with Hard X Rays, Phys. Rev. Lett. **117**, 113901 (2016).

[18] J. H. Shapiro, Computational ghost imaging, Phys. Rev. A **78**, 061802(R) (2008).

[19] X. Nie, X. Zhao, T. Peng, and M. O. Scully, Sub-Nyquist computational ghost imaging with orthonormal spectrum-encoded speckle patterns, Phys. Rev. A **105**, 043525 (2022).

[20] R. I. Khakimov, B. M. Henson, D. K. Shin, S. S. Hodgman, R. G. Dall, K. Baldwin, and A. G. Truscott, Ghost imaging with atoms, Nature (London) **540**, 100 (2016).

[21] W. Wan, C. Luo, F. Guo, J. Zhou, P. Wang, and X. Huang, Demonstration of asynchronous computational ghost imaging through strong scattering media, Opt. Laser Technol. **154**, 108346 (2022).

[22] F. Li, M. Zhao, Z. Tian, F. Willomitzer, and O. Cossairt, Compressive ghost imaging through scattering media with deep learning, Opt. Express **28**, 17395 (2020).

[23] Q. Fu, Y. Bai, X. Huang, S. Nan, P. Xie, and X. Fu, Positive influence of the scattering medium on reflective ghost imaging, Photonics Res. **7**, 1468 (2019).

[24] X. Shi, X. Huang, S. Nan, H. Li, Y. Bai, and X. Fu, Image quality enhancement in low-light-level ghost imaging using modified compressive sensing method, Laser Phys. Lett. **15**, 45204 (2018).

[25] Y. Yuan and H. Chen, Unsighted ghost imaging for objects completely hidden inside turbid media, New J. Phys. **24**, 43034 (2022).

[26] B. Liu, Z. Yang, S. Qu, and A. Zhang, Influence of turbid media at different locations in computational ghost imaging, Acta Opt. Sin. **36**, 1026017 (2016).

[27] M. Bina, D. Magatti, M. Molteni, A. Gatti, L. Lugiato, and F. Ferri, Backscattering Differential Ghost Imaging in Turbid Media, Phys. Rev. Lett. **110**, 083901 (2013).

[28] S. Liu, Z. Liu, J. Wu, E. Li, C. Hu, Z. Tong, X. Shen, and S. Han, Hyperspectral ghost imaging camera based on a flat-field grating, Opt. Express **26**, 17705 (2018).

[29] Y. Gao, X. Fu, and Y. Bai, Ghost imaging in transparent liquid, J. Opt. (Bristol, U. K.) **46**, 410 (2017).

[30] Y. Zhang, W. Li, H. Wu, Y. Chen, X. Su, Y. Xiao, Z. Wang, and Y. Gu, High-visibility underwater ghost imaging in low illumination, Opt. Commun. **441**, 45 (2019).

[31] M. Zhao, W. Yu, Z. Tian, and M. Zhao, Method of push-broom underwater ghost imaging computation, Laser Optoelectron. Prog. **56**, 161101 (2019).

[32] C. Luo, W. Wan, S. Chen, A. Long, L. Peng, S. Wu, and H. Qi, High-quality underwater computational ghost imaging with shaped Lorentz sources, Laser Phys. Lett. **17**, 105209 (2020).

[33] T. Wang, M. Chen, H. Wu, H. Xiao, S. Luo, and L. Cheng, Underwater compressive computational ghost imaging with wavelet enhancement, Appl. Opt. **60**, 6950 (2021).

[34] X. Yang, Z. Yu, L. Xu, J. Hu, L. Wu, C. Yang, W. Zhang, J. Zhang, and Y. Zhang, Underwater ghost imaging based on generative adversarial networks with high imaging quality, Opt. Express **29**, 28388 (2021).

[35] M. Le, G. Wang, H. Zheng, J. Liu, Y. Zhou, and Z. Xu, Underwater computational ghost imaging, Opt. Express **25**, 22859 (2017).

[36] M. Yin, L. Wang, and S. Zhao, Experimental demonstration of influence of underwater turbulence on ghost imaging, Chin. Phys. B **28**, 94201 (2019).

[37] Q. Zhang, W. Li, K. Liu, L. Zhou, Z. Wang, and Y. Gu, Effect of oceanic turbulence on the visibility of underwater ghost imaging, J. Opt. Soc. Am. A **36**, 397 (2019).

[38] Y. Wu, Z. Yang, and Z. Tang, Experimental study on anti-disturbance ability of underwater ghost imaging, Laser Optoelectron. Prog. **58**, 611002 (2021).

[39] Y. Liu, X. Liu, L. Liu, F. Wang, Y. Zhang, and Y. Cai, Ghost imaging with a partially coherent beam carrying twist phase in a turbulent ocean: A numerical approach, Appl. Sci. **9**, 3023 (2019).

[40] H. Wu, R. Wang, C. Li, M. Chen, G. Zhao, Z. He, and L. Cheng, Influence of intensity fluctuations on Hadamard-based computational ghost imaging, Opt. Commun. **454**, 124490 (2020).

[41] P. G. Vaz, D. Amaral, L. R. Ferreira, M. Morgado, and J. Cardoso, Image quality of compressive single-pixel imaging using different Hadamard orderings, Opt. Express **28**, 11666 (2020).

[42] X. Yu, R. I. Stantchev, F. Yang, and E. Pickwell-MacPherson, Super sub-Nyquist single-pixel imaging by total variation ascending ordering of the Hadamard basis, Sci. Rep.-UK **10**, 9338 (2020).

[43] W. Yu, Super sub-Nyquist single-pixel imaging by means of cake-cutting Hadamard basis sort, Sensors (Basel, Switzerland) **19**, 4122 (2019).

[44] P. G. Vaz, A. S. Gaudêncio, L. R. Ferreira, A. Humeau-Heurtier, M. Morgado, and J. Cardoso, Re-ordering of Hadamard matrix using Fourier transform and gray-level co-occurrence matrix for compressive single-pixel imaging in low resolution images, IEEE Access **10**, 46975 (2022).

[45] H. Wu, R. Wang, Z. Huang, H. Xiao, J. Liang, D. Wang, X. Tian, T. Wang, and L. Cheng, Online adaptive computational ghost imaging, Opt. Laser. Eng. **128**, 106028 (2020).

[46] L. Bian, J. Suo, Q. Dai, and F. Chen, Experimental comparison of single-pixel imaging algorithms, J. Opt. Soc. Am. A **35**, 78 (2018).

[47] C. Li, W. Yin, H. Jiang, and Y. Zhang, An efficient augmented Lagrangian method with applications to total variation minimization, Comput. Optim. Appl. **56**, 507 (2013).

[48] S. Gu, L. Zhang, W. Zuo, and X. Feng, Weighted nuclear norm minimization with application to image denoising, in *Proceedings of the IEEE Conference on Computer Vision and Pattern Recognition, Greater Columbus Convention Center in Columbus, Ohio, 23–28th June* (IEEE, Pisctaway, NJ, 2014), pp. 2862–2869.

[49] L. López-García, W. Cruz-Santos, A. García-Arellano, P. Filio-Aguilar, J. A. Cisneros-Martínez, and R. Ramos-García, Efficient ordering of the Hadamard basis for single pixel imaging, Opt. Express **30**, 13714 (2022).

[50] X. Yu, F. Yang, B. Gao, J. Ran, and X. Huang, Deep compressive single pixel imaging by reordering Hadamard basis: A comparative study, IEEE Access **8**, 55773 (2020).

[51] H. Wu, G. Zhao, R. Wang, H. Xiao, D. Wang, J. Liang, L. Cheng, and R. Liang, Computational ghost imaging system with 4-connected-region-optimized Hadamard pattern sequence, Opt. Laser. Eng. **132**, 106105 (2020).

[52] Z. Wang, A. C. Bovik, H. R. Sheikh, and E. P. Simoncelli, Image quality assessment: From error visibility to structural similarity, IEEE Trans. Image Process. **13**, 600 (2004).